



THE UNIVERSITY *of* EDINBURGH

Edinburgh Research Explorer

## **Synchrotron X-ray nanotomographic and spectromicroscopic study of the tricalcium aluminate hydration in the presence of gypsum**

**Citation for published version:**

Geng, G, Myers, RJ, Yu, Y-S, Shapiro, DA, Winarski, RP, Levitz, P, Kilcoyne, ALD & Monteiro, PJM 2018, 'Synchrotron X-ray nanotomographic and spectromicroscopic study of the tricalcium aluminate hydration in the presence of gypsum' *Cement and Concrete Research*, vol. 111, pp. 130-137. DOI: 10.1016/j.cemconres.2018.06.002

**Digital Object Identifier (DOI):**

[10.1016/j.cemconres.2018.06.002](https://doi.org/10.1016/j.cemconres.2018.06.002)

**Link:**

[Link to publication record in Edinburgh Research Explorer](#)

**Document Version:**

Peer reviewed version

**Published In:**

Cement and Concrete Research

**General rights**

Copyright for the publications made accessible via the Edinburgh Research Explorer is retained by the author(s) and / or other copyright owners and it is a condition of accessing these publications that users recognise and abide by the legal requirements associated with these rights.

**Take down policy**

The University of Edinburgh has made every reasonable effort to ensure that Edinburgh Research Explorer content complies with UK legislation. If you believe that the public display of this file breaches copyright please contact [openaccess@ed.ac.uk](mailto:openaccess@ed.ac.uk) providing details, and we will remove access to the work immediately and investigate your claim.



1  
2 **Synchrotron X-ray Nanotomographic and Spectromicroscopic Study of the**  
3 **Tricalcium Aluminate Hydration in the Presence of Gypsum**

4 Guoqing Geng<sup>1,2,\*</sup>, Rupert J. Myers<sup>1,3</sup>, Young-Sang Yu<sup>4</sup>, David A. Shapiro<sup>4</sup>, Robert  
5 Winarski<sup>5</sup>, Pierre E. Levitz<sup>6</sup>, David A.L. Kilcoyne<sup>4</sup>, Paulo J. M. Monteiro<sup>1,7</sup>

6 <sup>1</sup> Department of Civil and Environmental Engineering, University of California at  
7 Berkeley, Berkeley, California 94706, United States.

8 <sup>2</sup> Laboratory of Waste Management, Paul Scherrer Insitut, 5232 Villigen PSI,  
9 Switzerland

10 <sup>3</sup> University of Edinburgh, School of Engineering, King's Buildings, Sanderson Building,  
11 Edinburgh, EH9 3FB, United Kingdom.

12 <sup>4</sup> Advanced Light Source Lawrence Berkeley National Laboratory, Berkeley, California  
13 94720, United States.

14 <sup>5</sup> Center for Nanoscale Materials, Argonne National Laboratory, Argonne, Illinois 60439,  
15 United States.

16 <sup>6</sup> PHENIX lab, Sorbonne Université, UPMC Univ Paris 06, CNRS, Paris, France.

17 <sup>7</sup> Material Science Division-Lawrence Berkeley National Laboratory, Berkeley,  
18 California 94720, United States.

19 \* Correspondence and requests for materials should be addressed to Guoqing Geng  
20 (guoqing.geng@psi.ch).  
21

## 22 **Abstract**

23 The rheology of modern Portland cement (PC) concrete critically depends on the correct  
24 dosage of gypsum (calcium sulfate hydrate) to control the hydration of the most reactive  
25 phase - tricalcium aluminate ( $C_3A$ ). The underlying physio-chemical mechanism, however,  
26 remains unsolved mainly due to the lack of high-spatial-resolved and chemistry-sensitive  
27 characterization of the  $C_3A$  dissolution frontier. Here, we fill this gap by integrating  
28 synchrotron-radiation based crystallographic, photon-energy-dependent spectroscopic and  
29 high-resolution morphological studies of the  $C_3A$  hydration product layer. We propose that  
30 ettringite ( $6CaO \cdot Al_2O_3 \cdot SO_3 \cdot 32H_2O$ ) is the only hydration product after the initial reaction  
31 period and before complete gypsum dissolution. We quantify the 2D and 3D morphology  
32 of the ettringite network, e.g. the packing density of ettringite at various surface locations  
33 and the surface dissolution heterogeneity. Our results show no trace of a rate-controlling  
34 diffusion barrier. We expect our work to have significant impact on modeling the kinetics  
35 and morphological evolution of PC hydration.

36

## 37 **Key words**

38 Tricalcium Aluminate, Hydration Products, Characterization, X-Ray Diffraction,  
39 Spectromicroscopy.

40

## 41 **1. Introduction**

42 Portland cement (PC) concrete is ubiquitous. The centrality of this technology to modern  
43 society is attributed to the low cost and global availability of the raw materials used in PC  
44 manufacture (mainly limestone and clay) and concrete production (water and aggregate,

45 e.g., sand and stone), its robustness, controllability and high performance [1]. Precisely  
46 controlled rheology of fresh PC concrete is fundamentally important to produce high  
47 quality and durable PC concrete infrastructure, which is essential to reduce its  
48 environmental impact [1-4]. Gypsum ( $\text{CaSO}_4 \cdot 2\text{H}_2\text{O}$ ) addition is critical to control the  
49 fluidity and overall time window of flowability of fresh PC concrete mixtures to avoid  
50 ‘flash setting’ [1,4-6] by retarding the hydration of the most reactive PC clinker phase –  
51 tricalcium aluminate ( $\text{C}_3\text{A}$ ).

52 The hydration of  $\text{C}_3\text{A}$  can be delayed by minutes to hours depending on the  $\text{C}_3\text{A}$  to  
53 calcium sulfate ratio in cement [1,2,5]. The resulting period of low reactivity enables a  
54 fresh concrete mixture to be flowable; however, the chemistry underlying this mechanism  
55 has not been completely elucidated despite being researched for over half a century [5,7-  
56 19]. This uncertainty has mostly persisted because direct evidence of this mechanism has  
57 not been reported. Two main hypotheses exist, which describe the inhibition of  $\text{C}_3\text{A}$   
58 hydration to occur via: (i) the formation of an ettringite<sup>7</sup> ( $6\text{CaO} \cdot \text{Al}_2\text{O}_3 \cdot \text{SO}_3 \cdot 32\text{H}_2\text{O}$ )- and/or  
59 a Ca-Al layered double hydroxide (AFm, ‘alumino-ferrite-mono’)-type ‘diffusion barrier’  
60 that physically blocks the  $\text{C}_3\text{A}$  surface from contacting the aqueous phase. The AFm phases  
61 are reported as monosulfate ( $4\text{CaO} \cdot \text{Al}_2\text{O}_3 \cdot \text{SO}_3 \cdot 18\text{H}_2\text{O}$ , also denoted as s-AFm) [8] and/or  
62 hydroxyl AFm (OH-AFm, mainly  $4\text{CaO} \cdot \text{Al}_2\text{O}_3 \cdot 19\text{H}_2\text{O}$  ( $\text{C}_4\text{AH}_{19}$ ) [9,10], which dehydrates  
63 to  $4\text{CaO} \cdot \text{Al}_2\text{O}_3 \cdot 13\text{H}_2\text{O}$  ( $\text{C}_4\text{AH}_{13}$ ) at a relative humidity  $\sim 88\%$  [11,12], and gradually  
64 converts to  $3\text{CaO} \cdot \text{Al}_2\text{O}_3 \cdot 6\text{H}_2\text{O}$  ( $\text{C}_3\text{AH}_6$ ) over time [9]); or (ii) the adsorption of Ca and/or  
65 S complexes onto  $\text{C}_3\text{A}$  surface sites [13-15]. The latter hypothesis has recently gained  
66 increasing support although the ‘diffusion barrier’ hypothesis has not yet been disproven,  
67 due mainly to ettringite precipitates hindering a direct observation of the  $\text{C}_3\text{A}$  dissolution

68 frontier [16,17]. Therefore, a nanometer-resolved chemical-crystallographic probe is  
69 needed to more fully investigate the C<sub>3</sub>A dissolution frontier. Conventional imaging  
70 methods, including scanning electron microscopy (SEM) [18] and transmission electron  
71 microscopy (TEM) [19], are restricted by destructive sample preparation and electron beam  
72 damage. Three dimensional (3D) sub-micron scale characterization of the C<sub>3</sub>A dissolution  
73 frontier has also never been reported [20].

74 Recent advances in synchrotron-based experimental technology have substantially  
75 improved the ability to obtain direct chemical and morphological information in hydrated  
76 C<sub>3</sub>A systems: state-of-the-art soft X-ray ptychography imaging [21,22] coupled with  
77 scanning transmission X-ray microscopy (STXM), and X-ray adsorption near-edge fine  
78 structure (XANES) [23] now enables transmission imaging at ~5 nm pixel resolution and  
79 chemical (energy) mapping at ~70 nm pixel resolution [24,25], respectively. Here, we  
80 exploit this technology to reveal the mechanism by which C<sub>3</sub>A hydration is retarded in the  
81 presence of gypsum (with a C<sub>3</sub>A-to-gypsum mass ratio = 1 : 0.4, and a water-to-solid mass  
82 ratio = 10), aiming to identify features with sizes on the order of tens of nm at the C<sub>3</sub>A  
83 dissolution frontier. These data are complemented by three-dimensional (3D) tomograms  
84 reconstructed from full-field transmission X-ray microscopy (TXM) data at a voxel  
85 resolution ~20 nm<sup>3</sup> [26]. Crystallographic information is also obtained using in-situ wide  
86 angle X-ray scattering (WAXS). Small angle scattering (SAS) data is calculated from the  
87 X-ray ptychographic images [27,28] and compared with in-situ small angle X-ray  
88 scattering (SAXS) results, to obtain quantitative morphological information of the reacting  
89 C<sub>3</sub>A particle surface boundaries. The implications of these results on the contemporary

90 understanding of the dissolution-retarding effect of gypsum on C<sub>3</sub>A hydration, and on the  
91 computer-based cement hydration modeling are then discussed.

92

## 93 **2. Experimental**

### 94 **2.1 Materials**

95 Pure C<sub>3</sub>A and hydrogarnet (C<sub>3</sub>AH<sub>6</sub>) powders were purchased from Mineral Research  
96 Processing (<http://www.mineralresearchprocessing.fr/>). Gypsum was purchased from  
97 Fisher Scientific (#S76764). The purities of these materials were verified by powder X-ray  
98 diffraction (XRD) (see SI for details). The C<sub>3</sub>A powder has a size distribution from 1 μm  
99 to 100 μm, with  $d_{50} \sim 20 \mu\text{m}$  [15]. Partially-hydrated C<sub>3</sub>A samples were prepared by mixing  
100 gypsum, C<sub>3</sub>A and ‘nanopure’ water ( $1.82 \times 10^7 \Omega \text{ cm}$ , produced using a Barnstead  
101 NANOpure II with a filter size = 0.2 μm) in sealed plastic vials at room temperature ( $25 \pm$   
102  $2 \text{ }^\circ\text{C}$ ). The samples were agitated frequently by hand and/or constantly by mechanical  
103 rotation. An initial mass ratio of C<sub>3</sub>A to gypsum of 1 : 0.4 was used. A w/s = 10 was selected  
104 to fit the requirement of most experiments, and a w/s = 1 was also used for the X-ray  
105 ptychography experiments to verify the influence of sample dilution. Ettringite and s-AFm  
106 were independently prepared by precipitation from stoichiometric mixtures of C<sub>3</sub>A,  
107 gypsum and water, following the reported methods [29]. The identities of these reference  
108 minerals were confirmed by XRD, as shown in the Supplementary Information (SI).

### 109 **2.2 SEM**

110 C<sub>3</sub>A powder was spread on carbon tape pieces attached to steel SEM sample holders, which  
111 were then submerged into saturated gypsum-water solution. After certain hydration time  
112 (80s and 160s), the hydrated samples were then immediately rinsed with large quantities

113 of 99.5% ethanol and dried in N<sub>2</sub> atmosphere to prevent carbonation. Samples were carbon  
114 coated before observation, using a Zeiss EVO™ in second electron mode at 5 keV and 7  
115 pA.

### 116 **2.3 STXM and Al *K*-edge XANES**

117 The STXM experiments were conducted at beamline 5.3.2.1 of the ALS (Advanced Light  
118 Source) of LBNL (Lawrence Berkeley National Laboratory) [21], which operates at 1.9  
119 GeV and 500 mA using a bending magnet source and an active servo-stabilized toroidal  
120 pre-mirror that generates 10<sup>7</sup> photons per second at the sample location. The resolving  
121 power of the radiation source is  $E/\Delta E \sim 5000$ . Following the sample preparation method in  
122 previous work [30], partially hydrated C<sub>3</sub>A samples prepared as described above were  
123 drop-cast onto 100 nm-thick Si<sub>3</sub>N<sub>4</sub> windows (Norcada™), with excess solution removed  
124 using Kimwipes (Kimtech Science™). Samples were immediately transferred to the  
125 vacuumed STXM chamber. Single absorption contrast images were collected at an incident  
126 beam energy of 1575 eV (close to the Al *K*-edge). Stacks of absorption contrast images  
127 were recorded from 1552 to 1605 eV with step size 0.1 eV from 1565 to 1594 eV and step  
128 size 0.3 eV over the bordering central energy ranges of this investigation. A dwell time of  
129 3 s was used. The image stack was aligned and analyzed with the aXis2000 software [31].  
130 As reference minerals, hydrogarnet was dispersed with acetone whereas ettringite and s-  
131 AFm were dispersed with nanopure water, drop-cast and measured similarly. Internal  
132 calibration was conducted by calibrating the background absorption maximum to 1560 eV.

### 133 **2.4 X-ray ptychography**

134 X-ray ptychography imaging was conducted using the same STXM setup used for the Al  
135 *K*-edge XANES experiments. For these measurements, a 60 nm outer zone width zone plate

136 focused a coherent soft X-ray beam (750 eV) onto the sample, which was scanned in 40  
137 nm increments to ensure overlap of the probed areas. The effects of incoherent background  
138 signals were eliminated by implementing a background retrieval algorithm that iteratively  
139 determines a constant offset to the diffraction data. The sample was aligned with respect to  
140 the zone plate through an interferometric feedback system. A pixel size of 5 nm was used  
141 in image reconstruction. The efficient image resolution is determined to be ~17 nm by  
142 Fourier Ring Correlation (FRC; see SI for details) [32]. Small angle scattering calculations  
143 were performed using the ptychography images as input (the algorithm is available in SI).

#### 144 **2.5 In-situ WAXS and SAXS**

145 In-situ WAXS and SAXS experiments were conducted at the WAXS/SAXS beamline of  
146 the Synchrotron Light Research Institute (SLRI), Thailand, which runs at 1.2 GeV and 75-  
147 125 mA. For the measurements, an incident beam of 9 keV was transmitted through two  
148 pieces of kapton™ film between which the sample was placed, encompassing samples from  
149 2 to 120 minutes of hydration. The  $q$ -range covered was 0.04 to 42 nm<sup>-1</sup> for WAXS and  
150 0.07 to 0.7 nm<sup>-1</sup> for SAXS, both with an angular step size of 0.25°.

#### 151 **2.6 TXM tomography**

152 The TXM projections were collected at the Hard X-ray Nanoprobe Beamline, operated by  
153 the Center for Nanoscale Materials at Sector 26 of the Advanced Photon Source [26]. A  
154 cluster of partially-hydrated C<sub>3</sub>A samples was mounted on a tungsten needle tip and placed  
155 on a multi-directional scanning stage. The incident beam was tuned to 9 keV and condensed  
156 by an elliptically shaped single-reflection glass capillary with a central stop. Transmission  
157 images were recorded while the sample was rotated from -90° to 90°. Ten images were  
158 collected at every 1° step, with an exposure of 10 s at each step to obtain better statistics.



159 All tomographic 3D volume reconstructions were performed by an algebraic reconstruction  
160 technique (ART) with 20 iterations [33]; see details in SI.

161

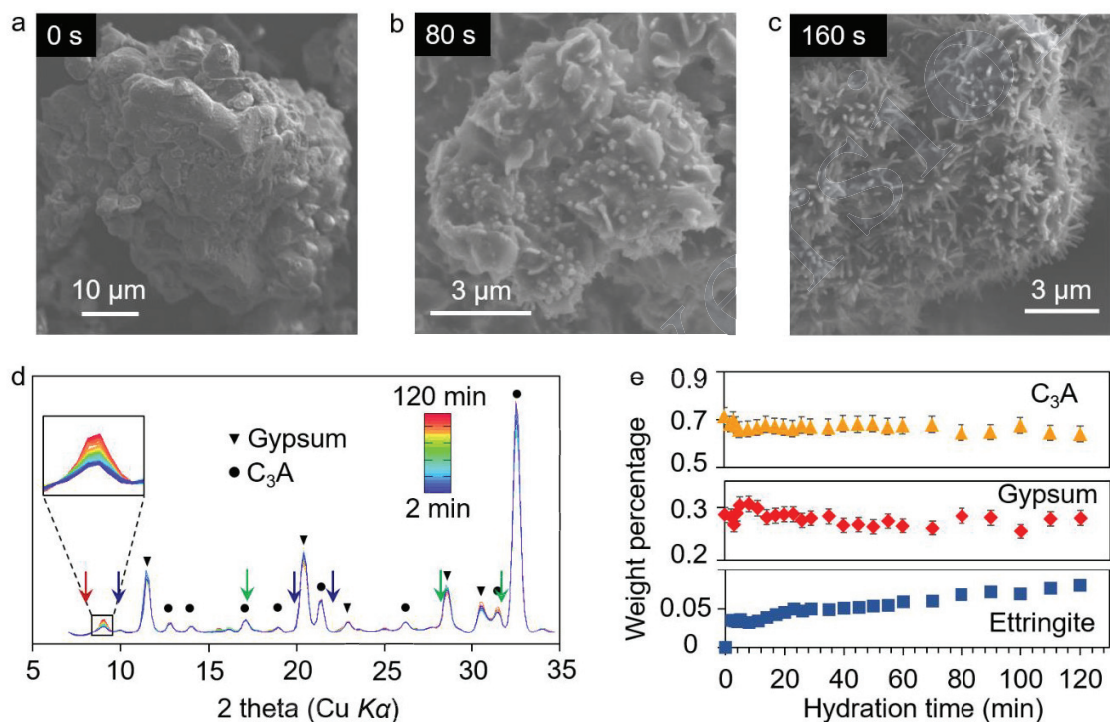
### 162 **3. Results**

163

#### 164 **3.1 In-situ WAXS study of the initial hydration.**

165 Fig. 1a-1c are the SEM images of the initial hydration of  $C_3A$  particles in calcium sulfate  
166 solution that is saturated with respect to gypsum. The surface morphology changes greatly  
167 over a few minutes. The first dominant hydration product has a foil/flake-like morphology,  
168 which coats the  $C_3A$  particles within the first minute ( $\leq 80$  s), but is then quickly masked  
169 by needle-like ettringite precipitates by 160 s (Fig. 1c). The initially formed flake-like  
170 precipitates are 200-300 nm thick at their edges (Fig. 1b) and are reported to be poorly-  
171 crystalline AFm phases [9,35]. The initial formed needles are short (Fig. 1b), but with  
172 similar diameter as the abundant ettringite that formed later on. Synchrotron-radiation  
173 based in-situ WAXS, with peaks assigned based on published results [36-41] detects only  
174 the diffraction of remnant  $C_3A$  and gypsum, and a small quantity of ettringite here, from 2  
175 to 120 minutes of hydration (Fig. 1d). The intensities of the major  $C_3A$  and gypsum  
176 diffraction peaks vary slightly with respect to the absolute values, whereas the intensity of  
177 ettringite diffraction increases monotonically with increasing hydration time (Fig. 1d,  
178 inset). The characteristic peaks of OH-AFm (e.g.,  $C_4AH_{19}$ ) at 10.7 Å, ( $8.3^\circ$ , red arrow in  
179 Fig. 1d) [39], and s-AFm at 8.97 Å ( $9.9^\circ$ , blue arrow in Fig. 1d) [40], are not observed  
180 during the first 120 minutes of hydration, indicating that the initially-formed AFm-type  
181 flakes, if initially formed, remain poorly crystalline, or are gradually decomposed with  
182 increasing hydration time. They do not seem to convert to  $C_3AH_6$  (4.44, 3.35 and 3.14 Å  
183 (i.e.  $20.1^\circ$ ,  $26.6^\circ$  and  $28.4^\circ$ , respectively, green arrows in Fig. 1d) [41]). A previous

184 synchrotron radiation XRD study of a similar system also revealed no trace of crystallized  
 185 AFm-type phases before gypsum is completely consumed [42]. However, AFm-type  
 186 crystals form immediately after mixing solid and water at a much lower initial gypsum-to-  
 187 C<sub>3</sub>A ratio [10]. It seems that the crystallinity of the AFm-type phase depends largely on the  
 188 dynamics of ion concentration change at the beginning of hydration.



189

190 **Fig. 1.** SEM and in-situ WAXS characterization of C<sub>3</sub>A hydration in the presence of gypsum.  
 191 SEM images of C<sub>3</sub>A particles before hydration (a), and hydrated for 80 s (b) and 160 s (c).  
 192 (d) In-situ WAXS results of a sample (C<sub>3</sub>A to gypsum mass ratio = 1 : 0.4) hydrated for 2 to  
 193 120 minutes, plotted in color series. C<sub>3</sub>A and gypsum diffraction peaks are labelled with  
 194 triangles and circles, respectively. The inset shows the evolution of the major diffraction peak  
 195 of ettringite. The red, blue and green arrows denote the unobserved characteristic diffraction  
 196 peaks of C<sub>4</sub>AH<sub>19</sub>, s-AFm and C<sub>3</sub>AH<sub>6</sub>, respectively. (e) Evolution of the mass percentages of  
 197 ettringite, gypsum and C<sub>3</sub>A during hydration determined using Rietveld refinement,  
 198 estimated relative error = ±5%.

199

200 Mass percentages of individual phases in the crystalline component of the reacted  
 201 sample are calculated through Rietveld refinement (Fig. 1d); see details in SI. A quick

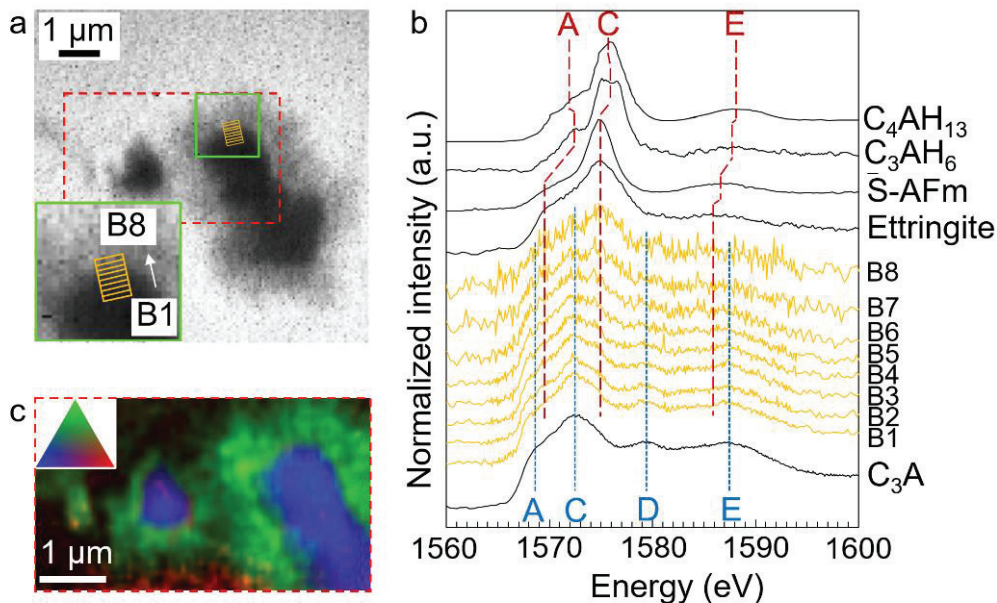
202 initial dissolution of  $C_3A$  is observed during the first 10 min. The dissolution of gypsum is  
203 slower with respect to  $C_3A$ , since the percentage of gypsum clearly rises within the first 10  
204 min. There is an initially observed ettringite formation ( $\sim 3.5$  wt%) at 2 min, which remains  
205 nearly unchanged within the first 10 min. Considering the low Al concentration in the  
206 liquid [16], the dissolved Al from  $C_3A$  most likely precipitates as Al-bearing phases of low  
207 sulfur content, for instance  $AH_3$  and AFm. This is consistent with the observation of  
208 previous in-situ XRD study on cement hydration [43,44]. After the first 10 min, a slow and  
209 steady rate of ettringite formation as well as gypsum and  $C_3A$  dissolution is observed, until  
210 120 min. Ettringite forms at a rate of  $\sim 2$  wt% per hour with respect to the total crystalline  
211 solid mass, reaching 8 wt% at 120 min. After 120 min hydration, the weight ratio of  
212 ettringite-to- $C_3A$  is 0.125 (Fig. 1e). The average diameter of  $C_3A$  particles is  $\sim 20$   $\mu m$  [15].  
213 If the surface of  $C_3A$  particle is smooth, the volume of ettringite divided by  $C_3A$  surface  
214 area is  $\sim 2.8$   $\mu m^3/\mu m^2$ , using the existing density data [36-37]. As shown in Fig. 1b, the  
215 formation of flake-like precipitates in the first minute precedes the significant precipitation  
216 of ettringite needles. Therefore, it is unlikely that they act as a physical barrier to retard the  
217 precipitation of ettringite within the first 2 minutes of hydration. However, it is still unclear  
218 whether an AFm-type layer persists as a physical barrier surrounding  $C_3A$  particles  
219 throughout the low-reactivity period, as it may be XRD-transparent, or masked by ettringite  
220 needles in the SEM images.

221

### 222 **3.2 XANES Spectromicroscopic study**

223 To further identify the solid phases, regardless of their crystallinity, on partly hydrated  $C_3A$   
224 surface, we collected the Al *K*-edge XANES spectra of eight regions parallel to the  $C_3A$

225 dissolution frontier (B1-B8 in Fig. 2a,) using nanometer resolved STXM. For comparison,  
226 XANES spectra of pure solid phases relevant to the  $C_3A$ -gypsum- $H_2O$  system were also  
227 measured and presented. In the Al  $K$ -edge XANES spectra, peaks A, C and E correspond  
228 to the transitions of  $1s$  to  $3s$ -like,  $3p$ -like and  $3d$ -like states, respectively, and peak D  
229 corresponds to multi-scattering within adjacent neighbor shells [45]. The transition of the  
230  $1s$  to the  $3s$  state is forbidden by the selection rule but is observable if the tetrahedron  
231 coordination is distorted and permits a mixture of Al  $s$  and  $p$  states, which is observed here.  
232 In good agreement with other Al-bearing minerals [45-48], the position of peak C, as shown  
233 in Fig. 2b, is a few eV lower for tetrahedral Al (Al[4]), i.e., in  $C_3A$  [36], than for octahedral  
234 Al (Al[6]), i.e., in solid hydration products such as ettringite [37], s-AFm [40],  $C_4AH_{13}$   
235 [11] (dehydration of  $C_4AH_{19}$  is likely to occur in vacuum conditions [12]) and  $C_3AH_6$  [41].  
236 The unique features of the reference spectra allow us to determine the identity of the solid  
237 hydration products.



239 **Fig. 2** STXM and Al K-edge XANES results for C<sub>3</sub>A hydrated for 150 minutes in the  
240 presence of gypsum. (a) An X-ray absorption contrast image at 1575 eV, with XANES data  
241 collected for each pixel (the pixel size is  $\sim 70 \times 70$  nm). Eight segments ( $\sim 100 \times 700$  nm  
242 each), marked by yellow rectangles labelled B1 (bottom) to B8 (top) (inset in a), are selected  
243 to sample a continuous region at the C<sub>3</sub>A dissolution frontier that includes unreacted C<sub>3</sub>A  
244 and solid hydration products (the inset is a magnification of the green-boxed region in the  
245 main image). (b) Al K-edge of XANES spectra for each area of B1-B8 (yellow curves), and  
246 the reference spectra for C<sub>3</sub>A and several possible Al-containing solid hydration products  
247 [2,4]. Resonance peaks for Al[4] and Al[6] are marked by short-dashed blue and long-dashed  
248 red lines, respectively. The spectrum of C<sub>4</sub>AH<sub>13</sub> is adapted from published work [47]. (c),  
249 Phase composition mapping of the region outlined by the dashed red rectangle in (a), where  
250 green, blue and red shaded areas correspond to ettringite, C<sub>3</sub>A and decomposition residue,  
251 respectively. Inset is a RGB color-triangle for reader convenience.

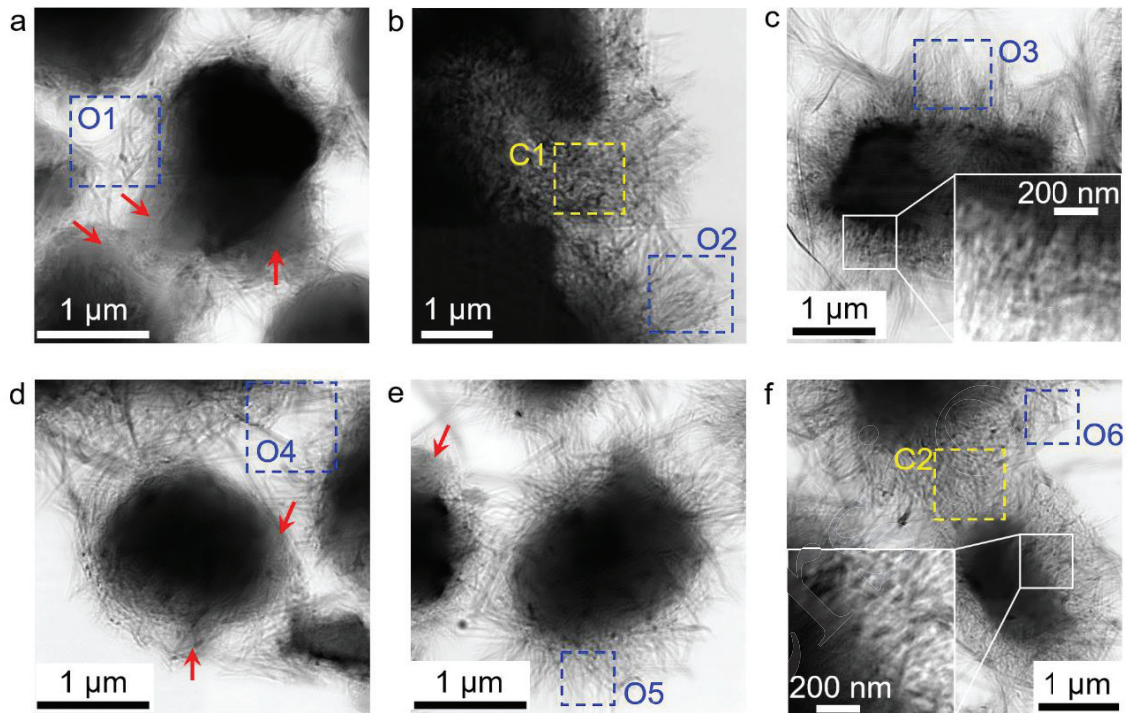
252  
253 In the Al K-edge XANES spectra of B1-B8, the intensities of the Al[4] peaks (blue short  
254 dashed lines) A (1568.6 eV), C (1572.5 eV), D (1579.3 eV) and E (1587.4 eV) shrink and  
255 the Al[6] peaks (red long dashed lines) C (1574.9 eV) and E (1585.9 eV) grow as functions  
256 of increasing distance away from the C<sub>3</sub>A particle (Fig. 2b). The spectra collected in  
257 regions B1 and B2 are almost identical to the Al K-edge XANES spectrum of C<sub>3</sub>A, which  
258 show strong intensities at the energies of its major tetrahedral Al (Al[4]) peaks A, C, D and  
259 E, indicating that these regions contain predominantly remnant C<sub>3</sub>A. The positions of the  
260 growing Al[6] peaks C and E in B1-B8 match with the corresponding peaks and positions  
261 for ettringite (1574.9 and 1585.9 eV respectively) rather than C<sub>3</sub>AH<sub>6</sub> (1576.0 and 1588.0  
262 eV respectively) or C<sub>4</sub>AH<sub>13</sub> (1575.8 and 1588.2 eV respectively). Compared to the  
263 intensities and shapes of peaks C and A in the spectrum for ettringite, peak C (1574.7 eV)  
264 is significantly sharper and peak a (1569.4 eV) is much weaker in the spectrum of s-AFm.  
265 Therefore, regions B3–B6 contain significant amounts of C<sub>3</sub>A (Al[4]) and ettringite (Al[6])  
266 and regions B7–B8 contain predominantly ettringite (Al[6]). After 150 minutes of  
267 hydration, ettringite is the only precipitate observed in the dissolution frontier of the C<sub>3</sub>A  
268 particle analyzed here.

269 The Al *K*-edge XANES of the full imaged region is well-fitted using the spectra of C<sub>3</sub>A  
270 (blue) and ettringite (green), with only a small residual signal (red) in the background  
271 region that is thus assigned to measurement noise (Fig. 2c). This result further demonstrates  
272 that ettringite is the only solid hydration product here at 150 minutes of hydration. There  
273 is no trace of AFm phases, although flake-like AFm dominate the surface morphology at  
274 initial hydration (Fig. 1b). There is also no trace of C<sub>3</sub>AH<sub>6</sub> that is expected to precipitate  
275 from the destabilization of OH-AFm phases. This ettringite layer is ~1 μm thick on the  
276 bigger C<sub>3</sub>A particle (Fig. 2a, right), and slightly thinner on the smaller one (Fig. 2a, left).

277

### 278 **3.3 Quantifying nano-morphology using X-ray ptychographic imaging and in-situ** 279 **SAXS**

280 X-ray ptychographic imaging is used to observe the morphology of the C<sub>3</sub>A dissolution  
281 frontier (Fig. 3). The image resolution is determined to be ~17 nm by Fourier ring  
282 correlation; see SI. Needle-like ettringite precipitates studied here are observed with similar  
283 thickness from 30 to 620 minutes of hydration in the water to solid mass ratio (w/s) = 10  
284 system (Fig. 3a-3c). The population of ettringite needles increases with increasing  
285 hydration time, but individual needles generally all grow to a maximum length of ~1 μm  
286 and do not seem to thicken significantly. Ettringite prefers to nucleate on C<sub>3</sub>A particles,  
287 and generally grow perpendicular to the C<sub>3</sub>A surface (dashed blue squares). The needle  
288 network is increasingly densified through interlacing of ettringite needles in confined  
289 regions (dashed yellow squares). By 620 minutes of hydration, the layer of ettringite  
290 needles are observed to directly contact the remnant C<sub>3</sub>A surface, i.e., no continuous  
291 physical barrier is observed in the interfacial zone (inset in Fig. 3c).



292

293 **Fig. 3** X-ray ptychographic images of  $C_3A$  hydrated in the presence of gypsum and  $w/s = 10$   
 294 (a-c), and  $w/s = 1$  (d-f), at hydration times of: (a) 30 min; (b) 135 min; (c) 620 min; (d) 30  
 295 min; (e) 90 min; and (f) 910 min. The pixel size is  $5 \times 5 \text{ nm}^2$ . Blue and yellow squares indicate  
 296 needle-like ettringite precipitation on open  $C_3A$  surfaces and confined spaces between  
 297 particles, respectively. Red arrows indicate a gel-like hydration product that is observed at  
 298 early hydration only. The insets in c and f are magnified regions of the interface between  
 299 remnant  $C_3A$  and hydration product (white boxes).

300

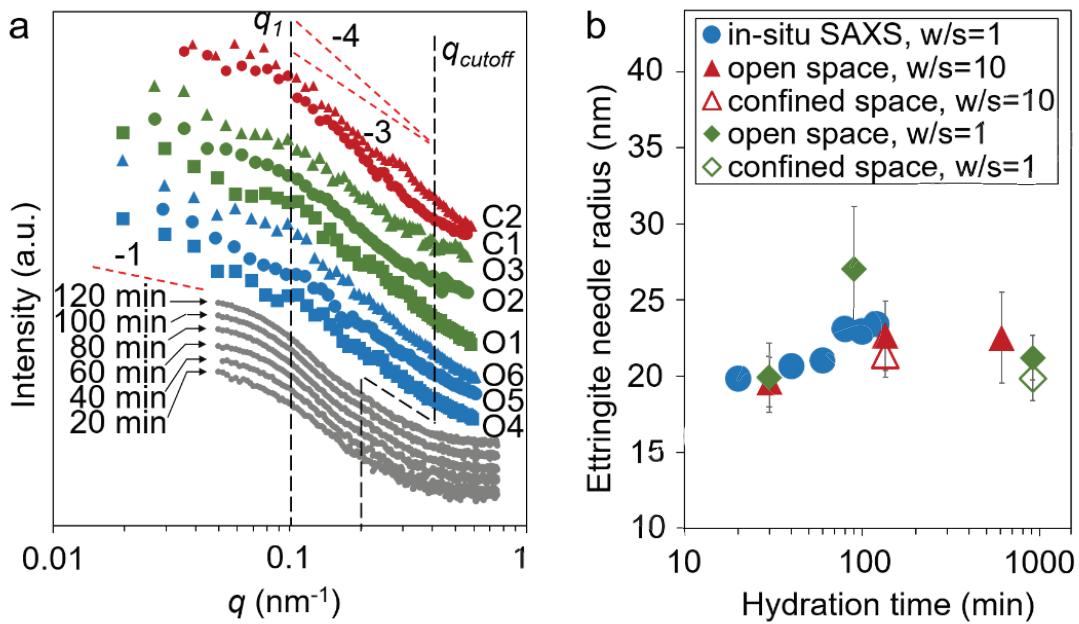
301 The morphologies of the  $C_3A$  dissolution frontier in the  $w/s = 10$  (Fig. 3a-3c) and  $w/s =$   
 302 1 (Fig. 3d-3f) systems are similar. Ettringite needles reach a length of  $\sim 1 \mu\text{m}$  after 910  
 303 minutes of hydration and thicken negligibly in the  $w/s = 1$  system. A solid ‘diffusion  
 304 barrier’ is not identified at 910 minutes of hydration (Fig. 3f inset).  $C_3A$  hydration kinetics  
 305 is reported to be independent of the  $w/s$  between 1 and 10 [16,49]. In both  $w/s$  systems,  
 306 there exist continuous ‘gel-like’ areas (red arrows in Fig. 3a, 3d and 3e) on the particle  
 307 surfaces that have distinct grey scale values compared to the remnant  $C_3A$  and with  
 308 dimension of a few hundred nanometers. They are observed to be abundant at a relatively

309 early age of hydration, and intermixed with ettringite needles on the C<sub>3</sub>A surface. These  
310 gel-like morphologies are highly consistent with the flake-like AFm gel as shown in SEM  
311 images (Fig. 1b). However, this gel is not observed at a later age of hydration under the  
312 transmission microscope (Fig. 3b, 3c and 3f), indicating that the initially formed AFm  
313 flakes are unstable, and may dissolve to feed the precipitation of ettringite during the low-  
314 reactivity period. Therefore, the initially formed AFm gel is unable to act as the physical  
315 barrier described in the ‘diffusion barrier’ hypothesis to retard C<sub>3</sub>A dissolution throughout  
316 the low-reactivity period as stated in the introduction. This interpretation is consistent with  
317 the STXM and Al *K*-edge XANES results.

318 To quantify the morphology of the ettringite needles that precipitate under different  
319 degrees of spatial confinement, theoretical calculations of SAS (algorithm available in SI)  
320 are applied to the selected dashed blue (O1-O6, less confined) and yellow (C1-C2, more  
321 confined) square regions in Fig. 3, and are compared with in-situ SAXS measurements of  
322 the  $w/s = 1$  system (Fig. 4). The calculated SAS results generally resemble the in-situ SAXS  
323 results, and both can be interpreted using the form factor of a typical Guinier-Porod pattern  
324 of agglomerated isometric rods or cylinders [50]. This provides strong evidence that the  
325 needle-like morphology of ettringite at the C<sub>3</sub>A dissolution frontier is not an artefact of  
326 drying, which is suggested to alter the surface morphology of hydrated PC particles [51].  
327 In a log-log plot of the intensity vs. scattering vector ( $q$ ), the  $q_1$  and  $q_{cutoff}$  values define the  
328 lower and higher end, respectively, of a linear Porod region with slope between -4 and -3,  
329 corresponding to the surface fractal dimension. For  $q < q_1$ , a nonlinear Guinier region with  
330 slope ranging from -1 to -3 is inferred, which corresponds to the volume fractal dimension.  
331 Due to the limitation of the SAXS experimental setup and the overall size of the selected



332 ptychographic image regions ( $\sim 1 \mu\text{m}^2$  here), the low- $q$  end of the Guinier region here is not  
 333 small enough to reliably probe the length scale equal to or larger than the needle length  
 334 (i.e.,  $> \sim 1 \mu\text{m}$ ).



335

336 **Fig. 4** Quantifying the morphology of  $\text{C}_3\text{A}$  particles hydrated in the presence of gypsum  
 337 using SAS. (a) In-situ SAXS results from 20 to 120 minutes of hydration, using the SAXS at  
 338 a hydration time of 2 minutes as the background signal, which is comprised mainly of liquid  
 339 water,  $\text{C}_3\text{A}$  and gypsum. SAS were also calculated from the regions marked by dashed  
 340 squares in the ptychographic images (Fig. 3). The  $q_1$  (intersection between lower- $q$  Guinier  
 341 region and higher- $q$  Porod region) and  $q_{cutoff}$  (high- $q$  end of Porod region) are schematically  
 342 marked with black long-dashed lines. Red short-dashed lines with slope -4 and -3 are  
 343 displayed as eye guides only. (b) Evolution of the radii of the needle-like ettringite  
 344 precipitates, with the uncertainty denoted by error bars and marker size. The uncertainty is  
 345 derived from the fitting of  $q_1$  and  $d$ .

346

347 As shown in Fig. 1c and Fig. 3, the needle-like ettringite precipitates are similarly sized.

348 In an isometric rod model, the radius ( $r$ ) of the rod can be related to  $q_1$  following eq.(1)

349 [50]:

350 
$$q_1 = (2d-2)^{0.5}/r \quad (1)$$

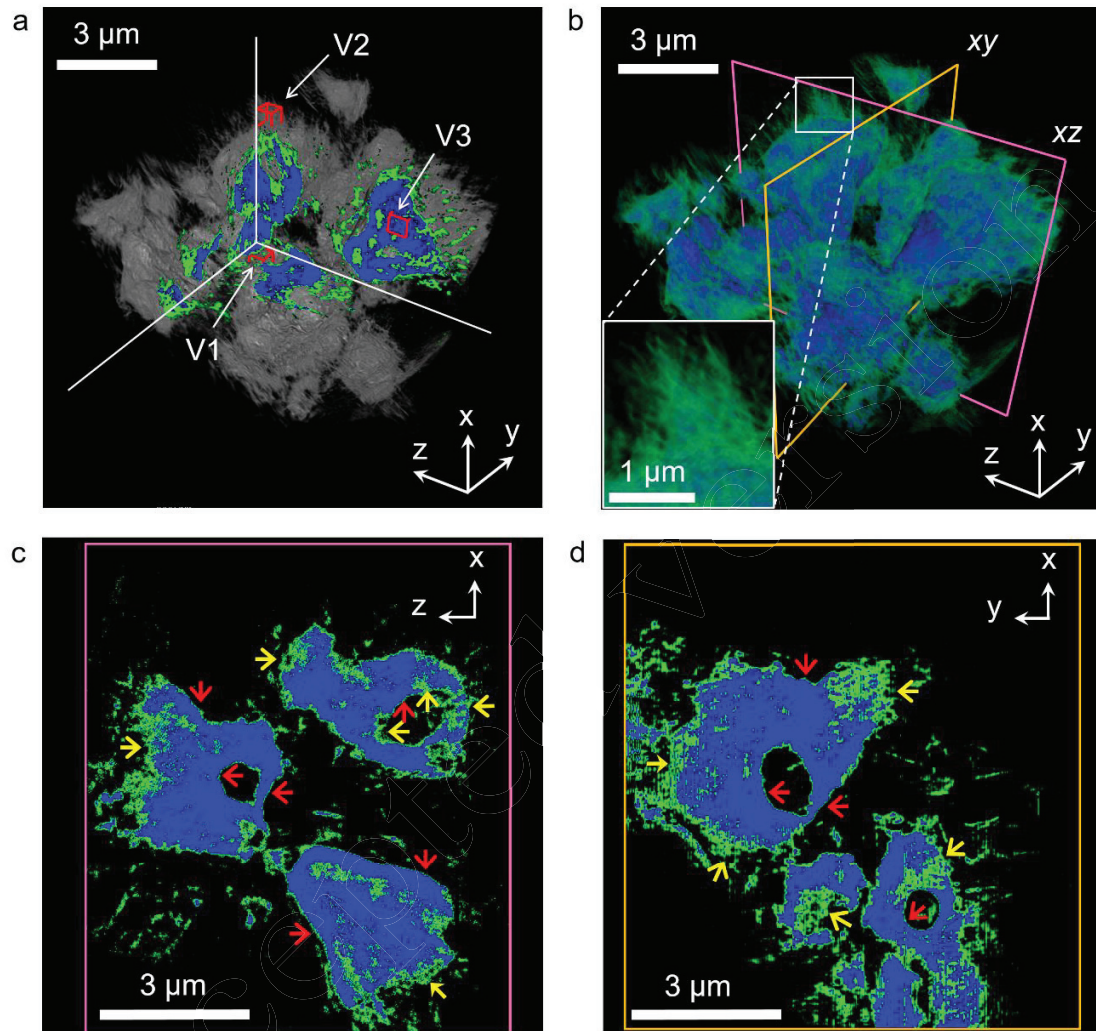
351 where  $d$  is the fractal dimension of the Porod region (further details regarding the  
352 interpretation of the SAXS data are presented in the SI), i.e., the absolute value of the slope  
353 when the logarithm of the intensity (base 10) is plotted as a function of  $q$  (Fig. 4a). The  
354 fitted needle radius,  $r$ , from the in-situ SAXS measurement increases slightly as a function  
355 of hydration time, i.e., from  $\sim 20$  nm at 20 minutes of hydration to  $\sim 23$  nm at 120 minutes  
356 of hydration, with a standard error of  $\sim 0.7$  nm (Fig. 4b). A comparable result was obtained  
357 from the SAS data calculated from the ptychographic images at both  $w/s = 1$  and 10, where  
358 the radii of ettringite crystallites was determined to be  $\sim 23 \pm 5$  nm (Fig. 4b). Needles in  
359 confined space (C1-C2) are of similar thickness to those growing in open space (O1-O6).  
360 Therefore, before complete dissolution of gypsum (i.e.,  $< \sim 10$  hours), the typical radius of  
361 ettringite precipitates is  $< 30$  nm, and is independent of the  $w/s$  and hydration time; similarly  
362 the aspect ratio of ettringite needles is generally around 40. As hydration progresses, the  
363 growth of ettringite crystals is mainly through new precipitates on the  $C_3A$  surface, rather  
364 than the thickening or lengthening of individual ettringite needles.

365

### 366 **3.4 Quantifying 3D morphology using nano-CT**

367 To date, only 2D nano- and meso-scale morphologies of hydrated  $C_3A$  have been reported,  
368 providing limited morphological information on the  $C_3A$  dissolution frontier. To further  
369 probe the 3D nano-scale morphology of the  $C_3A$  dissolution frontier, a full-field TXM  
370 tomographic study was conducted to yield a 3D image at a voxel resolution of 20 nm, as  
371 shown in Fig. 5, where the blue and green colors represent  $C_3A$  and ettringite, respectively.  
372 A movie of the volume rendering is presented in the SI. The segmentation of the

373 background, ettringite and remnant  $C_3A$  was based on the reconstructed optical density  
374 ( $OD_{recon}$ ) histogram of the 3D image. Further details of the procedures are in the SI.



375

376 **Fig. 5** 3D reconstruction of  $C_3A$  particles hydrated for 143 minutes in the presence of gypsum.  
377 (a) A cubic sub-volume (white lines represent its edges) is removed from the full 3D dataset  
378 to expose interior features, which are colored blue (remnant  $C_3A$ ) and green (solid hydration  
379 products). The reconstructed voxel volume is  $20 \times 20 \times 20 \text{ nm}^3$ . Sub-volumes V1, V2 and V3  
380 (unfilled red cubes of 600 nm edge length) correspond to hydration products grown in  
381 confined space, open space, and remnant  $C_3A$ , respectively. (b) Colored volume rendering  
382 of remnant  $C_3A$  (blue) and hydration product (green). A magnified region is shown in the  
383 white box inset. Two slices, marked by pink and orange squares, are displayed in (c) (xz  
384 plane) and (d) (xy plane), respectively. Segmentation of hydration products and remnant  $C_3A$   
385 is performed by applying a threshold optical density value according to the histogram of the  
386 full 3D data (further details are available in the SI).

387

388 As calculated from the segmented 3D image, the volume of the ettringite and remnant  
389  $C_3A$  are  $\sim 40 \mu\text{m}^3$  and  $\sim 52 \mu\text{m}^3$ , respectively. By simplifying the  $C_3A$  particles in Fig. 5 as  
390 4 agglomerated particles with roughly spherical shape and smooth surface, the total surface  
391 area of  $C_3A$  is  $\sim 27 \mu\text{m}^2$ . The volume of ettringite to the calculated surface area of remnant  
392  $C_3A$  is thus  $\sim 1.5 \mu\text{m}^3/\mu\text{m}^2$ . This value is in the same order of magnitude as estimated using  
393 quantitative analysis of WAXS data, i.e.  $\sim 2.8 \mu\text{m}^3/\mu\text{m}^2$ , and therefore suggests that the  
394 segmentation is reasonable. However, by directly counting the surface area using the  
395 segmented 3D image of  $C_3A$ , its surface area is  $\sim 249 \mu\text{m}^2$ , which is one magnitude larger  
396 than the estimated value by assuming a smooth  $C_3A$  surface. This discrepancy indicates  
397 that the partially dissolved  $C_3A$  surface is very rough.

398 The result shows that  $C_3A$  particles are non-uniformly reacted at 143 minutes of  
399 hydration (Fig. 5), with the solid hydration products on  $C_3A$  surfaces varying in thickness  
400 up to 1-1.5  $\mu\text{m}$ , with some surface areas barely covered. This information is not observed  
401 in the 2D X-ray ptychographic images (Fig. 3) as they are transmission images.  
402 Heterogeneous  $C_3A$  dissolution is observed to generate sub-micron scale features,  
403 including highly reacted and rough surface regions (yellow arrows in Fig. 5c and 5d) and  
404 much smoother surfaces with low reaction extents (red arrows in Fig. 5c and 5d). There  
405 seems to be no intermediate status, i.e., the  $C_3A$  surface either dissolves extensively to form  
406 needle-like precipitations of constant maximum length ( $\sim 1.5 \mu\text{m}$ ), or stays almost  
407 unreacted. From a visual estimation, the highly dissolved  $C_3A$  surface area is about 40%  
408 of its total surface area at a hydration age of 143 min. In some low-reaction surface regions,  
409 the green color layer is of single voxel thickness, which is not necessarily a thin layer of

410 ettringite. In fact, the transmission images with higher resolution shown no evidence of  
411 such continuous layers (Fig. 3c and 3f). Therefore they are most-likely due to artifacts of  
412 the segmentation due to the voxels on the C<sub>3</sub>A surface containing both solid and void  
413 regions.

414 Surfaces of inner cavities are also reactive. Any originally closed cavities participate in  
415 hydration as soon as the dissolution frontier exposes them to the solution. Non-uniform  
416 hydration is also observed in the inner cavities of remnant C<sub>3</sub>A particles (Fig. 5c and 5d),  
417 some of which are more connected to the external particle surface than others. The amount  
418 of reactive C<sub>3</sub>A surface is directly related to the speed of ettringite formation [16]. Here,  
419 the TXM results show that the significant proportion of C<sub>3</sub>A surface reacts at very slow  
420 rate which highlights the non-uniform nature of C<sub>3</sub>A surface dissolution and hydration,  
421 observed on both external surface and internal cavity surface.

422 Porosities of selected sub-volumes in Fig. 5a, V1 (solid hydration products grown in  
423 confined space), V2 (solid hydration products grown in open space) and V3 (remnant C<sub>3</sub>A),  
424 are determined according to the attenuation law [52]. In the SI, we show that the porosity,  
425  $\varphi$ , can be estimated using eq.(2):

$$426 \quad \varphi = 1 - OD_{recon\_mean} / OD_{recon\_max} \quad (2)$$

427 where  $OD_{recon\_mean}$  is the average reconstructed optical density of the studied sub-volumes,  
428 and  $OD_{recon\_max}$  is the reconstructed optical density of a zero-porosity voxel of the studied  
429 phase (ettringite or C<sub>3</sub>A); see further details in the SI. By applying this equation to the three  
430 sub-volumes, we determine the respective porosities of V1, V2 and V3 to be 53-67%, 73-  
431 81% and 20%-38%. Therefore, after 143 minutes of hydration, the network of ettringite  
432 needles in open C<sub>3</sub>A spaces (V2) is highly porous, and the network of ettringite needles in

433 confined spaces (V1) is denser but also significantly porous. The region representing  
434 remnant C<sub>3</sub>A (V3) contains non-zero porosity that may be caused by the presence of initial  
435 cavities.

436 The porosity of the cementitious binder critically influences its physical properties, and  
437 is therefore a key target of hydration modelling [1,2]. In a randomly packed rod network,  
438 the volume fraction of solid rods decreases with their increasing aspect ratio, reaching  
439 ~10% when the aspect ratio is ~40 [53]. Here, the volume fractions of ettringite needles on  
440 C<sub>3</sub>A surface estimated using the 3D image is ~2-5 times the value in the randomly packed  
441 case, indicating that the ettringite needles are systematically oriented. Previous studies of  
442 ettringite-water suspension indicate that the ettringite volume fraction  $\phi$  and the rod aspect  
443 ratio are related to various rheological properties such as suspension viscosity and the onset  
444 rate of shear thinning [54]. Therefore, this characterization of porosity and hydration  
445 product geometry on the sub-30 nm length scale, the first of its kind, can be used to develop  
446 and validate detailed 3D computational models of C<sub>3</sub>A hydration, nano-structure and  
447 rheology, a substantial step-change to a higher level of detail compared to existing  
448 formulations.

449  
450

## 451 **5. Discussion**

452

453 Our results provide strong evidence that OH-AFm and s-AFm do not greatly retard the  
454 initial formation of ettringite as ettringite forms rapidly after a few minutes of hydration  
455 when most of the C<sub>3</sub>A surface is already covered by amorphous AFm phases. These AFm  
456 phases also do not form a C<sub>3</sub>A dissolution-inhibiting ‘diffusion-barrier’ in the low-  
457 reactivity period, because ettringite is identified by coupled STXM and Al K-edge XANES

458 as the only precipitate on C<sub>3</sub>A particles after 150 minutes of hydration, but before complete  
459 gypsum dissolution. The initially formed AFm phases destabilize completely to ettringite  
460 during the low-reactivity period. At an imaging resolution of ~15 nm, no obvious  
461 'diffusion-barrier' is observed at the C<sub>3</sub>A dissolution frontier after the initial hydration  
462 period. Our X-ray ptychography and TXM results also show that the ettringite needle  
463 network at the C<sub>3</sub>A dissolution frontier is highly porous. The porosities of this network are  
464 53-67% and 73-81% in confined and open spaces after 143 min of hydration, respectively,  
465 meaning that it does not act as a physical barrier to retard C<sub>3</sub>A hydration, in contradiction  
466 to the 'diffusion barrier' hypothesis. Therefore, the results point toward an alternative  
467 mechanism of C<sub>3</sub>A dissolution retardation, e.g., by adsorption of Ca and/or S complexes  
468 onto C<sub>3</sub>A surface sites [8,15,55].

469 The morphology of the C<sub>3</sub>A dissolution frontier in the presence of gypsum in aqueous  
470 solution is similar in systems with w/s = 1 and 10. In both cases, ettringite precipitation  
471 predominantly occurs via the production of more individual surface-bound needles rather  
472 than the existing needles increasing in thickness and length. Ettringite needles with radii of  
473 ~20 nm are observed after 20 min of hydration and grow to ~25 nm thick by 15 hours  
474 hydration; and the length of individual ettringite needles remain ~1 μm. The independence  
475 of the needle size on the w/s suggests that it is not the free space which determines the size  
476 of needle. The growth of ettringite needles may be determined by the solution chemistry  
477 facts close to nucleation sites, instead of the bulk liquid region far away from C<sub>3</sub>A surface.  
478 A maximum growth length is also observed for the hydration products of tricalcium silicate  
479 (C<sub>3</sub>S), calcium silicate hydrates, which is suggested to be merely determined by the  
480 solution chemistry [56].

481 On the other hand, the 3D image clearly indicates that the  $C_3A$  surface either undergoes  
482 substantial dissolution to form needles of 1-1.5  $\mu\text{m}$  length, or otherwise stays essentially  
483 unreacted. This heterogeneity indicates that  $C_3A$  dissolution is also somewhat controlled  
484 by its crystalline surface chemistry and morphology [55]. Similar observation was reported  
485 recently for the hydration of a polished  $C_3A$  surface [57]. The dissolution of mineral  
486 surfaces are often promoted by the surface concentration of defects, such as roughness,  
487 grain boundaries and dislocations [58]. As indicated by Fig. 5, the dominating surface  
488 defect seems to be heterogeneously distributed at the micron-scale, and varies from facets  
489 to facets of the  $C_3A$  particles. This could be either the difference of roughness (amount of  
490 kinks) created during the grinding process, or the different cleavages (with different  
491 dissolution rate) created during the sintering process. However, we are unable to identify  
492 individual surface defects due to the limit of resolution.

493 Upon the above discussion, we now have a general picture of the studied reaction. When  
494  $C_3A$  surface is in contact with sulfur-containing water solution, it undergoes quick  
495 dissolution and formation of an AFm-type gel, followed by the long low-reactivity period.  
496 In the low-reactivity period, the AFm-type gel quickly vanishes, and  $C_3A$  surface  
497 dissolution is very slow probably due to ion-complexation. Along with the slow  
498 dissolution, as soon as a defect site is exposed to solution, there is a localized quick  
499 dissolution of  $C_3A$ , followed by the quick growth of ettringite until a certain size. In the  
500 surface regions where less defects exist, ettringite formation is hardly observed. In future  
501 work, two processes need urgent investigation in order to quantitatively predict the  $C_3A$   
502 hydration: 1) the dissolution of a single defect site on  $C_3A$  surface, 2) the mechanism that  
503 ettringite only grows to a certain size.



504 For the first time, this paper provides a sub-30 nm 2D and 3D morphological and  
505 spectroscopic study of the C<sub>3</sub>A dissolution frontier in the presence of gypsum during the  
506 low-reactivity period. It advances the understanding of cubic C<sub>3</sub>A hydration in the presence  
507 of gypsum, through the central quantification of the chemistry and morphology of  
508 hydration product on C<sub>3</sub>A surface. This work also serves as a preliminary step to studying  
509 PC hydration with sub-30 nm resolution synchrotron radiation technologies. We expect  
510 that these techniques will provide key experimental evidence to validate multi-scale  
511 computational simulations of PC hydration down to the nano-scale [59-61], and also the  
512 macro-scale properties of fresh PC concrete [54,62].

513

#### 514 **Supporting information**

515

516 The supporting information available as a separate file, which includes the characterization  
517 of the raw materials, process of analyzing the WAXS and SAXS data, reconstruction and  
518 segmentation of the 3D TXM result, estimating the resolution of the ptychography images,  
519 and determining the peak positions of the XANES results. A video of the 3D rendering of  
520 the TXM result is also provided.

521

#### 522 **Acknowledgments**

523

524 This work is funded by the Singapore-Berkeley Building Efficiency and Sustainability in the  
525 Tropics (SinBerBEST) Program. The authors acknowledge the support received from  
526 Ubonwan Khopongpaiboon, Panod Viseshchitra and Thanakrit Chantra (Siam Cement,  
527 Thailand), and from Siriwat Soontaranon (SAXS beamline of Synchrotron light research  
528 institute, Thailand). The Advanced Light Source was supported by the Director, Office of

529 Science, Office of Basic Energy Sciences, of the U.S. Department of Energy under Contract  
530 No. DE-AC02-05CH11231. Use of the Center for Nanoscale Materials and the Advanced  
531 Photon Source, both Office of Science user facilities, was supported by the U.S. Department  
532 of Energy, Office of Science, Office of Basic Energy Sciences, under Contract No. DE-  
533 AC02-06CH11357. The authors want to acknowledge Jeffrey W. Bullard (NIST, USA) for  
534 the insightful discussion on  $C_3A$  hydration. Guoqing Geng's PhD study is supported by the  
535 Chinese Scholarship Council (file No. 201206090127).

536

### 537 **References**

538

- 539 1. P.K. Mehta, P.J.M. Monteiro, Concrete Microstructure, Properties, and Materials,  
540 McGraw-Hill Companies, New York City, ed. 4, 2014.
- 541 2. P. Barnes, J. Bensted, Structure and Performance of Cements, CRC Press, Boca Raton,  
542 ed. 2, 2002.
- 543 3. G.P. Peters, G. Marland, C. Le Quéré, T. Boden, J. G. Canadell, M. R. Raupach, Rapid  
544 growth in CO<sub>2</sub> emissions after the 2008-2009 global financial crisis. Nature Clim.  
545 Change. 2 (2012) 2-4.
- 546 4. Mehta, P. K. Reducing the Environmental Impact of Concrete. Concr. Int. 23 (2001)  
547 61-66.
- 548 5. H.F.W. Taylor, Cement Chemistry; Thomas Telford: London, 2<sup>nd</sup> edition, 1997.
- 549 6. E.B. Nelson, Well Cementing. Development of Petroleum Science, Vol. 28; Newnes:  
550 Boston, MA, 1990.
- 551 7. M. Collepardi, G. Baldini, M. Pauri, M. Corradi, Tricalcium aluminate hydration in  
552 the presence of lime, gypsum or sodium sulfate. Cem. Concr. Res. 8 (1978) 571-580.

- 553 8. J.W. Bullard, H.M. Jennings, R.A. Livingston, A. Nonat, G.W. Scherer, J.S.  
554 Schweitzer, K.L. Scrivener, J.J. Thomas, Mechanisms of cement hydration. *Cem.*  
555 *Concr. Res.* 41 (2011) 1208-1223.
- 556 9. L. Black, C. Breen, J. Yarwood, C.S. Deng, J. Phipps, G. Maitland, Hydration of  
557 tricalcium aluminate ( $C_3A$ ) in the presence and absence of gypsum — studied by  
558 Raman spectroscopy and X-ray diffraction. *J. Mater. Chem.* 16 (2006) 1263-1272.
- 559 10. A.N. Christensen, T.R. Jensen, N.V. Scarlett, I.C. Madsen, J.C. Hanson, Hydrolysis of  
560 pure and sodium substituted calcium aluminates and cement clinker components  
561 investigated by in situ synchrotron X-ray powder diffraction. *J. Am. Ceram. Soc.* 87  
562 (2004) 1488-1493.
- 563 11. E. Aruja, The unit cell and space group of  $4CaO \cdot Al_2O_3 \cdot 19H_2O$  polymorphs. *Acta*  
564 *Cryst.* 14 (1961) 1213-1216.
- 565 12. M.H. Roberts, New calcium hydrates. *J. Appl. Chem.* 7 (1957) 543-546.
- 566 13. M.E. Tadros, W.Y. Jackson, J. Skalny, Study of the dissolution and electrokinetic  
567 behavior of tricalcium aluminate. *Colloid Interface Sci.* 4 (1976) 211-223.
- 568 14. J. Skalny, M.E. Tadros, Retardation of tricalcium aluminate hydration by sulfates. *J.*  
569 *Am. Ceram. Soc.* 60 (1977) 174-175.
- 570 15. R.J. Myers, G. Geng, J. Li, E. D. Rodríguez, J. Ha, P. Kidkhunthod, G. Sposito, L.N.  
571 Lammers, A. P. Kirchheim, P. J. M. Monteiro, The role of adsorption phenomena in  
572 cubic tricalcium aluminate dissolution. *Langmuir*, 33 (2016) 45-55.
- 573 16. H. Minard, S. Garrault, L. Regnaud, A. Nonat, Mechanisms and parameters controlling  
574 the tricalcium aluminate reactivity in the presence of gypsum. *Cem. Concr. Res.* 37  
575 (2007) 1418-1426.

- 576 17. A. Quennoz, K.L. Scrivener, Hydration of  $C_3A$  – gypsum systems. *Cem. Concr.*  
577 *Res.* 42 (2012) 1032-1041.
- 578 18. R. Holly, H. Peemoeller, M. Zhang, E. Reardon, C. M. Hansson, Magnetic resonance  
579 in situ study of tricalcium aluminate hydration in the presence of gypsum. *J. Am.*  
580 *Ceram. Soc.* 89 (2006) 1022-1027.
- 581 19. C.J. Hampson, J.E. Bailey, The Microstructure of the hydration products of tri-calcium  
582 aluminate in the presence of gypsum. *J. Mater. Sci.* 18 (1983) 402-410.
- 583 20. M.D. Jackson, J. Moon, E. Gotti, R. Taylor, S.R. Chae, M. Kunz, A.H. Emwas, C.  
584 Meral, P. Guttman, P. Levitz, H.R. Wenk, Material and elastic properties of Al-  
585 tobermorite in ancient Roman seawater concrete. *J. Am. Ceram. Soc.* 96 (2013) 2598-  
586 2606.
- 587 21. D.A. Shapiro, Y.S. Yu, T. Tyliczszak, J. Cabana, R. Celestre, W. Chao, K.  
588 Kaznatcheev, A.L.D. Kilcoyne, F. Maia, S. Marchesini, Y.S. Meng, Chemical  
589 composition mapping with nanometre resolution by soft X-ray microscopy. *Nature*  
590 *Photon.* 8 (2014) 765-769.
- 591 22. Y.S. Yu, C. Kim, D.A. Shapiro, M. Farmand, D. Qian, T. Tyliczszak, A.D. Kilcoyne,  
592 R. Celestre, S. Marchesini, J. Joseph, P. Denes, Dependence on crystal size of the  
593 nanoscale chemical phase distribution and fracture in  $Li_xFePO_4$ . *Nano Lett.* 15 (2015)  
594 4282-4288.
- 595 23. A.L.D. Kilcoyne, T. Tyliczszak, W.F. Steele, S. Fakra, P. Hitchcock, K. Franck, E.  
596 Anderson, B. Harteneck, E.G. Rightor, G.E. Mitchell, A.P. Hitchcock, Interferometer-  
597 controlled scanning transmission X-ray microscopes at the Advanced Light Source. *J.*  
598 *Synchrotron Radiat.* 10 (2003) 125-136.

- 599 24. G. Geng, R. Taylor, S. Bae, D. Hernández-Cruz, A.L.D. Kilcoyne, A.H. Emwas,  
600 P.J.M. Monteiro, Atomic and nano-scale characterization of a 50-year-old hydrated  
601 C<sub>3</sub>S paste. *Cem. Concr. Res.* 77 (2015) 36-46.
- 602 25. G. Geng, J. Li, Y. S. Yu, D.A. Shapiro, A.L.D. Kilcoyne, P.J.M. Monteiro, Nanometer-  
603 resolved spectroscopic study reveals the conversion mechanism of CaO·Al<sub>2</sub>O<sub>3</sub>·10H<sub>2</sub>O  
604 to 2CaO·Al<sub>2</sub>O<sub>3</sub>·8H<sub>2</sub>O and 3CaO·Al<sub>2</sub>O<sub>3</sub>·6H<sub>2</sub>O at an elevated temperature. *Cryst.*  
605 *Growth Des.* 17 (2017) 4246-4253.
- 606 26. R.P. Winarski, M.V. Holt, V. Rose, P. Fuesz, D. Carbaugh, C. Benson, D. Shu, D.  
607 Kline, G.B. Stephenson, I. McNulty, J.A. Maser, Hard X-ray nanoprobe beamline for  
608 nanoscale microscopy. *J. Synchrotron Radiat.* 19 (2012) 1056-1060.
- 609 27. S. Brisard, R.S. Chae, I. Bihannic, L. Michot, P. Guttmann, J. Thieme, G. Schneider,  
610 P.J.M. Monteiro, P. Levitz, Morphological quantification of hierarchical geomaterials  
611 by X-ray nano-CT bridges the gap from nano to micro length scales. *Am. Mineral.* 97  
612 (2012) 480-483.
- 613 28. P. Levitz, D. Tchoubar, Disordered porous solids: from chord distributions to small  
614 angle scattering. *J. Phys. I.* 2, (1992) 771-790.
- 615 29. T. Matschei, B. Lothenbach, F.P. Glasser, The AFm Phase in Portland Cement, *Cem.*  
616 *Concr. Res.* 37 (2007) 118-130.
- 617 30. G. Geng, R. J. Myers, A.L. Kilcoyne, J. Ha, P.J.M. Monteiro, Ca L<sub>2,3</sub>-edge near edge  
618 X-ray absorption fine structure of tricalcium aluminate, gypsum and calcium  
619 (sulfo)aluminate hydrates. *Am. Mineral.* 102 (2017) 900-908.

- 620 31. A.P. Hitchcock, P. Hitchcock, C. Jacobsen, C. Zimba, B. Loo, E. Rotenberg, J.  
621 Denlinger, R. Kneedler, aXis 2000 — Analysis of X-ray images and spectra.  
622 <http://unicorn.mcmaster.ca/aXis2000.html>.
- 623 32. M. Van Heel, M. Schatz, Fourier shell correlation threshold criteria. *J. Struct.*  
624 *Biol.* 151 (2005) 250-262.
- 625 33. R. Gordon R. Bender, G.T. Herman, Algebraic reconstruction techniques (ART) for  
626 three-dimensional electron microscopy and X-ray photography. *J. Theor. Biol.* 29  
627 (1970) 471-481.
- 628 34. A.C. Kak, M. Slaney, Principles of Computerized Tomographic Imaging, Society for  
629 Industrial and Applied Mathematics, Philadelphia, 2001.
- 630 35. P. Meredith, A.M. Donald, N. Meller, C. Hall, Tricalcium aluminate hydration:  
631 microstructural observations by in-situ electron microscopy. *J. Mater. Sci.* 39 (2004)  
632 997-1005.
- 633 36. P. Mondal, J.W. Jeffery, The crystal structure of tricalcium aluminate,  $\text{Ca}_3\text{Al}_2\text{O}_6$ . *Acta*  
634 *Cryst. B* 31 (1975) 689-697.
- 635 37. A.E. Moore, H.F.W. Taylor, Crystal Structure of Ettringite. *Acta Cryst. B* 26 (1970)  
636 386-393.
- 637 38. P. Comodi, S. Nazzareni, P.F. Zanazzi, S. Speziale, High-pressure behavior of  
638 gypsum: a single-crystal X-ray study. *Am. Mineral.* 93 (2008) 1530-1537.
- 639 39. T.R. Jensen, A.N. Christensen, J.C. Hanson, Hydrothermal transformation of the  
640 calcium aluminum oxide hydrates  $\text{CaAl}_2\text{O}_4 \cdot 10\text{H}_2\text{O}$  and  $\text{Ca}_2\text{Al}_2\text{O}_5 \cdot 8\text{H}_2\text{O}$  to  
641  $\text{Ca}_3\text{Al}_2(\text{OH})_{12}$  investigated by in situ synchrotron X-ray powder diffraction. *Cem.*  
642 *Concr. Res.* 35 (2005) 2300-2309.

- 643 40. R. Allmann, Refinement of the hybrid layer structure  $[\text{Ca}_2\text{Al}(\text{OH})_6] \cdot [1/2\text{SO}_4 \cdot 3\text{H}_2\text{O}]^+$ .  
644 Neues. Jb. Miner. Monat. 3 (1977) 136-144.
- 645 41. G.A. Lager, T. Armbruster, J. Faber, Neutron and X-ray diffraction study of  
646 hydrogarnet  $\text{Ca}_3\text{Al}_2(\text{O}_4\text{H}_4)_3$ . Am. Mineral. 72 (1987) 756-765.
- 647 42. M. Merlini, G. Artioli, T. Cerulli, F. Cella, A. Bravo, Tricalcium aluminate hydration  
648 in additivated systems. A crystallographic study by SR-XRPD. Cem. Concr. Res. 38  
649 (2008) 477-486.
- 650 43. C. Hesse, F. Goetz-Neunhoeffler, J. Neubauer, A new approach in quantitative in-situ  
651 XRD of cement pastes: Correlation of heat flow curves with early hydration  
652 reactions. Cem. Concr. Res. 41 (2011) 123-128.
- 653 44. D. Jansen, F. Goetz-Neunhoeffler, C. Stabler, J. Neubauer. A remastered external  
654 standard method applied to the quantification of early OPC hydration. Cem. Concr.  
655 Res. 41 (2011) 602-608.
- 656 45. D. Li, G.M. Bancroft, M. Fleet, X. Feng, Y. Pan, Al K-edge XANES spectra of  
657 aluminosilicate minerals. Am. Mineral. 80 (1995) 432-440.
- 658 46. D.R. Neuville, G.S. Henderson, L. Cormier, D. Massiot, The structure of crystals,  
659 glasses, and melts along the  $\text{CaO-Al}_2\text{O}_3$  join: results from Raman, Al L- and K-edge  
660 X-ray absorption, and  $^{27}\text{Al}$  NMR spectroscopy. Am. Mineral. 95 (2010) 1580-1589.
- 661 47. M. Vespa, E. Wieland, R. Dähn, D. Grolimund, A.M. Scheidegger, Determination of  
662 the elemental distribution and chemical speciation in highly heterogeneous  
663 cementitious materials using synchrotron-based micro-spectroscopic  
664 techniques. Cem. Concr. Res. 37 (2007) 1473-1482.

- 665 48. N. Richard, N. Lequeux, P. Boch, EXAFS study of refractory cement phases:  
666  $\text{CaAl}_2\text{O}_4$ ,  $\text{Ca}_2\text{Al}_2\text{O}_7$ , and  $\text{Ca}_3\text{Al}_2\text{O}_8$ . J. Phys. III 5 (1995) 1849-1864.
- 667 49. N. Tenoutasse, The hydration mechanism of  $\text{C}_3\text{A}$  and  $\text{C}_3\text{S}$  in the presence of calcium  
668 chloride and calcium sulfate. Proceedings of the 5<sup>th</sup> International Symposium on the  
669 Chemistry of Cement, 1968.
- 670 50. B. Hammouda, New Guinier-Porod Model. J. Appl. Cryst. 43 (2010) 716-719.
- 671 51. P.C. Fonseca, H.M. Jennings, The effect of drying on early-age Morphology of C-S-  
672 H as observed in environmental SEM. Cem. Concr. Res. 40 (2010) 1673-1680.
- 673 52. J.H. Hubbell, S.M. Seltzer, Tables of X-ray Mass Attenuation Coefficients 1 keV to  
674 20 MeV for Elements Z=1 to 92 and 48 Additional Substances of Dosimetric Interest,  
675 National Institute of Standards and Technology, Interagency/Internal Report 5632,  
676 Gaithersburg, 1995.
- 677 53. A.P. Philipse, The random contact equation and its implications for (colloidal) rods in  
678 packings, suspensions, and anisotropic powders. Langmuir, 12 (1996)1127-1133.
- 679 54. C.M. Vladu, C. Hall, G.C. Maitland, Flow properties of freshly prepared ettringite  
680 suspensions in water at 25° C. J Colloid Interface Sci. 294 (2006) 466-472.
- 681 55. W. Stumm, Reactivity at the mineral-water interface: dissolution and inhibition.  
682 Colloids Surf. A 120 (1997) 43-166.
- 683 56. K.L. Scrivener, P. Juilland, P.J.M. Monteiro, Advances in understanding hydration of  
684 portland cement. Cem. Concr. Res. 78 (2015) 38-56.
- 685 57. A.S. Brand, J.W. Bullard, Dissolution kinetics of cubic tricalcium aluminate measured  
686 by digital holographic microscopy. Langmuir. 8 (2017).



- 687 58. A. Lüttge, R.S. Arvidson, C.A. Fischer, Stochastic treatment of crystal dissolution  
688 kinetics. *Elements*. 9 (2013) 183-188.
- 689 59. D.P. Bentz, Three-dimensional computer simulation of portland cement hydration and  
690 microstructure development. *J. Am. Ceram. Soc.* 80 (1997) 3-21.
- 691 60. S. Bishnoi, K.L. Scrivener, *mic*: A new platform for modelling the hydration of  
692 cements. *Cem. Concr. Res.* 39 (2009) 266-274.
- 693 61. J.W. Bullard, E. Enjolras, W.L. George, S.G. Satterfield, J.E. Terrill, A parallel  
694 reaction-transport model applied to cement hydration and microstructure  
695 development. *Model. Simul. Mater. Sci. Eng.* 18 (2010) 025007.
- 696 62. F.J. Ulm, O. Coussy, Modeling of thermochemomechanical couplings of concrete at  
697 early ages. *J. Eng. Mech-ASCE*. 121 (1995) 785-794.

accepted revision